



An analogue twin for piezoelectric vibration damping of multiple nonlinear resonances

Boris Lossouarn ^{a,*}, Gaetan Kerschen ^b, Jean-François Deü ^a

^a Laboratoire de Mécanique des Structures et des Systèmes Couplés (LMSSC), Conservatoire national des arts et métiers (Cnam), 292 Rue Saint-Martin, Paris, 75003, France

^b Department of Aerospace and Mechanical Engineering, University of Liège, Allée de la Découverte, 9, Liège, B-4000, Belgium

ARTICLE INFO

Keywords:

Vibration damping
Piezoelectric coupling
Broadband control
Nonlinear resonances

ABSTRACT

The objective of this study is to extend the concept of analogous piezoelectric networks to vibration mitigation of multiple nonlinear resonances. First, the undamped linear part of the electrical network is designed so as to possess similar modal characteristics as those of the underlying linear mechanical structure. Then, nonlinear electrical components possessing the same mathematical form as that of the mechanical nonlinearities are added to the network. Because both modal and nonlinear analogies are enforced, the electrical network can be seen as an analogue twin of the mechanical structure. When the network is coupled to the structure via an array of piezoelectric elements, it is shown numerically and experimentally that such an analogue twin offers important benefits for vibration mitigation over a broad range of frequencies and excitation amplitudes.

1. Introduction

Looking back over the origins of analogue electronics offers the opportunity to remember that, initially, the word *analogue* was not related to a continuously variable signal but to a real analogy between physical quantities. Indeed, before the appearance of *digital computers* in the 1960s, *analogue computers* based on electrical networks were able to simulate the dynamics of complex systems ruled by differential equations [1,2]. In structural dynamics, the “Cal Tech Electric Analog Computer” [3] was used to build a reduced-order model of an airplane in order to simulate flutter instabilities [4]. McNeal contributed significantly to this prolific field of research before the increasing power of *digital computers* finally encouraged him to develop the finite element (FE) method for structural analysis, which resulted in the NASTRAN computer program [5].

The FE method enabled the creation of what was later called a *digital twin* [6] capable of reproducing the dynamics of a real structure in a virtual domain synthesized by a digital computer. The paradigm was different with the analogue case because the computer and the twin were actually the same physical object allowing real-time measurements of the simulated physical quantities. Analogue computers became obsolete before the 1970s, but the corresponding analogous electrical networks were revived in the 2000s for the purpose of vibration absorption [7–9]. Indeed, coupling a mechanical structure to an electrical network possessing similar modal properties can achieve broadband vibration mitigation.

Based on recent developments with analogous piezoelectric networks [10–12] and with piezoelectric nonlinear vibration absorbers [13–16], the central contribution of this paper is to develop an *analogue twin* of a nonlinear mechanical structure, i.e., a fully passive analogous electrical network that mimics the dynamics of the host structure. We note that the word *analogue* recovers

* Corresponding author.

E-mail address: boris.lossouarn@lecnam.net (B. Lossouarn).

herein its present meaning, i.e. a continuously variable signal, whereas the word *twin* refers to the analogy. The electromechanical analogy beyond the linear regime is ensured by adopting the principle of similarity proposed in [17], i.e., a nonlinearity possessing the same mathematical form as that of the mechanical nonlinearity is introduced in the analogous electrical network. Doing so, vibration mitigation of nonlinear resonances can be achieved over a broad range of frequencies and excitation amplitudes.

The paper is organized as follows. The main principles of piezoelectric shunt damping of a single linear resonance are first recalled in Section 2. The extension to vibration mitigation of multiple linear resonances through the use of analogous electrical networks is then discussed. The concept was recently applied to various linear structures [12], but another contribution of the present paper is to provide a clear framework for optimizing modal damping over a broad frequency range by the introduction of adequate electrical resistances. Section 3 introduces the concept of an analogue twin of a nonlinear host structure and validates it numerically using a piezoelectric beam with a cubic nonlinearity. The experimental demonstration of the proposed developments is carried out in Section 4. The electromechanical parameters of the experimental piezoelectric beam are first identified before an analogous electrical network with a nonlinear capacitor is coupled to the beam. Finally, the conclusions of the study are drawn in Section 5.

2. Vibration mitigation based on analogous piezoelectric coupling

2.1. Single mode damping with a linear piezoelectric tuned vibration absorber

The resonant piezoelectric shunt [18], also called piezoelectric tuned vibration absorber, is used to reduce the vibration amplitude of a single linear resonance. It generally comprises a piezoelectric transducer of capacitance C^* at zero strain connected to an inductance L^* and a series resistance R^* . Considering a single-degree-of-freedom mechanical system coupled to such a resonant shunt, the governing equations of motion are

$$\begin{bmatrix} m^* & 0 \\ 0 & L^* \end{bmatrix} \begin{bmatrix} \ddot{u} \\ \ddot{q} \end{bmatrix} + \begin{bmatrix} c^* & 0 \\ 0 & R^* \end{bmatrix} \begin{bmatrix} \dot{u} \\ \dot{q} \end{bmatrix} + \begin{bmatrix} k^* + \frac{e^2}{C^*} & -\frac{e}{C^*} \\ -\frac{e}{C^*} & \frac{1}{C^*} \end{bmatrix} \begin{bmatrix} u \\ q \end{bmatrix} = \begin{bmatrix} f \\ 0 \end{bmatrix}, \quad (1)$$

where u represents the mechanical displacement, q is the electrical charge displacement and f is the excitation force. The constants m^* , c^* , k^* , and e are the modal mass, damping coefficient, stiffness in short circuit and coupling coefficient, respectively. A piezoelectric coupling factor is commonly defined as

$$k_c = \frac{e}{\sqrt{k^* C^*}} = \sqrt{\frac{\omega_0^2 - \omega_s^2}{\omega_s^2}} \quad \text{where} \quad \omega_s = \sqrt{\frac{k^*}{m^*}} \quad \text{and} \quad \omega_0 = \sqrt{\frac{k^* + \frac{e^2}{C^*}}{m^*}}, \quad (2)$$

ω_s and ω_0 being the natural angular frequencies in short and open circuit. The inductance and resistance values

$$L^* = \frac{1}{C^* \omega_0^2} \quad \text{and} \quad R^* = \sqrt{\frac{3}{2}} \frac{k_c}{C^* \omega_0} \quad (3)$$

minimize the maximum of the dynamic compliance frequency response function (FRF) [19,20]. We note that Eq. (3) provides a sufficient approximation of the optimal resistance when dealing with reasonable values of the coupling factor $k_c \leq 0.2$.

2.2. Vibration mitigation of multi-resonant structures

The extension of resonant piezoelectric shunts to multimodal structures consists in designing a multi-resonant circuit whose electrical natural frequencies are sufficiently close to the mechanical resonances to be controlled. By analogy with a mechanical structure, one can define for each electrical mode i a modal inductance L_i^* , a modal capacitance C_i^* and a modal damping ratio ξ_{ei} . In order to be tuned to the natural angular frequencies in open circuit ω_{oi} , the electrical network has to satisfy

$$L_i^* C_i^* = \frac{1}{\omega_{oi}^2} \quad \text{and} \quad \xi_{ei} = \sqrt{\frac{3}{8}} k_{ci} \quad (4)$$

for all the mechanical resonances to be damped. These two optimal conditions directly come from Eq. (3) and the definition of an optimal quality factor

$$\frac{1}{2\xi_{ei}} = \frac{L_i^* \omega_{oi}}{R_i^*} = \sqrt{\frac{2}{3}} \frac{1}{k_{ci}}. \quad (5)$$

With a single piezoelectric transducer, the most direct approach is the so-called multi-branch shunt [15,21,22] made of inductors and capacitors organized with just as many branches as the number of targeted mechanical resonances. Because the addition of external capacitors in the shunt decreases electromechanical coupling [23] and because the positioning of a single piezoelectric patch is generally not optimal for different mode shapes [24], this solution does not provide the best coupling factors k_{ci} for all the considered modes.

Another solution for multimodal damping is based on analogous piezoelectric coupling [8–12]. This technique requires several piezoelectric transducers that are interconnected with electrical components so as to build a multi-resonant network with modal

Table 1
Dimensions and properties for the beam and the piezoelectric patches.

	Beam (Steel)	Patches (PZT 5A)
Length	$l_b = 700$ mm	$l_p = 67$ mm
Width	$b = 14$ mm	$b = 14$ mm
Thickness	$h_b = 14$ mm	$h_p = 2$ mm
Second moment of area	$I_b = \frac{bh_b^3}{12} = 3201$ mm ⁴	$I_p = \frac{b(h_b+2h_p)^3 - h_b^3}{24} = 1801$ mm ⁴
Density	$\rho_b = 7850$ kg/m ³	$\rho_p = 7800$ kg/m ³
Young's modulus	$Y_b = 210$ GPa	$Y_p^E = 66$ GPa
End stiffness	$k^{\text{end}} = 3810$ N/m	–
Permittivity	–	$\epsilon_{33}^\sigma = 1800\epsilon_0 = 16$ nF/m
Charge constant	–	$d_{31} = -190$ pC/N

properties similar to those of the considered structure. The analogy is no more restrained to the natural frequencies (as with the multi-branch shunts) but similar mode shapes are also ensured, which justifies the denomination as an *analogue twin*. We note that the analogy is strictly valid only for the undamped dynamics because large damping is to be deliberately introduced in the electrical network to cause vibration mitigation.

2.3. Analogous electrical network for a beam

The structure under consideration in this paper is a beam whose dimensions and material properties are given in Table 1. One end of the beam is fully clamped whereas the other end is equipped with a thin lamina that generates an additional stiffness k^{end} . The design of an electrical analogue for beam structures is fully described in [10] but the main steps of the method are recalled in this section for completeness.

First, the fourth-order partial differential equation that defines the dynamics of an Euler–Bernoulli beam is considered :

$$YI \frac{\partial^4 q_w}{\partial x^4} + \rho S \ddot{q}_w = 0, \quad (6)$$

where q_w is the transverse displacement, \ddot{q}_w its second time derivative, x corresponds to the longitudinal direction and t to the time. ρ is the density of the beam, S is the cross-sectional area, Y is the Young's modulus, and I is the second moment of area. Three new variables q_θ , V_θ and V_w are introduced to obtain an equivalent formulation with first-order spatial derivatives:

$$q_\theta = \frac{\partial q_w}{\partial x}, \quad V_\theta = -YI \frac{\partial q_\theta}{\partial x} \quad \text{and} \quad V_w = -\frac{\partial V_\theta}{\partial x}, \quad (7)$$

which implies

$$\rho S \ddot{q}_w = -\frac{\partial V_w}{\partial x}. \quad (8)$$

These continuous equations can be spatially discretized with a finite difference scheme, leading to

$$\begin{aligned} L \ddot{q}_{wI} &= V_{wL} - V_{wR}, & V_{\theta I} &= \frac{1}{C} (q_{\theta L} - q_{\theta R}), \\ \frac{\hat{a}}{2} V_{wL} &= V_{\theta L} - V_{\theta I}, & \frac{\hat{a}}{2} q_{\theta L} &= q_{wI} - q_{wL}, \\ \frac{\hat{a}}{2} V_{wR} &= V_{\theta I} - V_{\theta R}, & \frac{\hat{a}}{2} q_{\theta R} &= q_{wR} - q_{wI}. \end{aligned} \quad (9)$$

where \hat{a} is the discretization step between the left and the right sides, denoted 'L' and 'R' respectively, and 'I' corresponds to the internal equidistant position. The set of Eqs. (9) is represented by the electrical unit cell drawn in Fig. 1 (with $R_L = R_C = R_T = 0$), which is finally equivalent to a discrete beam segment. The analogous electrical unit cell is made of an inductance $L = \rho S \hat{a}$ representing the analogue of a point mass and the capacitance $C = \hat{a}/YI$ represents a bending compliance. There is also a transformer of ratio \hat{a} that is analogous to a mechanical lever having the length of the discretization step.

The complete analogous network is built by reproducing this unit cell along one direction, taking into account that the number of unit cells per wavelength has to be sufficiently large to approximate the continuous mechanical medium. The electrical analogue of a beam with $n = 10$ unit cells is represented in Fig. 2. In order to approximate the mode shapes of a cantilever beam, we also need to ensure analogous boundary conditions. This is realized by short-circuiting one end of the network (equivalent to zero force and moment) while leaving open the other end (equivalent to zero displacement and angle). Another critical condition is the tuning of the dispersion relation in the electrical waveguide. From the discrete model, it can be shown that the electrical parameters do not necessarily have to be equal to their electrical analogues as long as they satisfy

$$\frac{1}{\hat{a}^2} \frac{1}{LC} = \frac{1}{a^2} \frac{k_\theta}{m}, \quad (10)$$

where k_θ is the bending stiffness of the mechanical unit cell, m is its mass and $a = l_b/n$ its length [10].

The following step is to couple the considered mechanical beam to its analogous electrical network with an array of piezoelectric patches. Thanks to the inherent capacitance C of the piezoelectric patches, there is no need for external capacitors for the analogue of the bending stiffness. Only transformers and inductors satisfying Eq. (10) are required for the analogue of a clamped beam. In

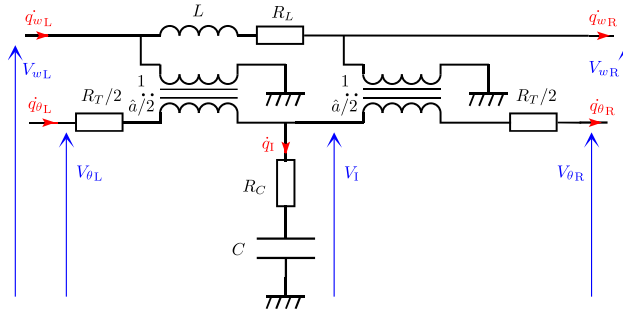


Fig. 1. Electrical beam unit cell with damping components.

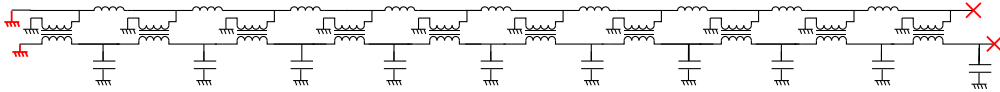
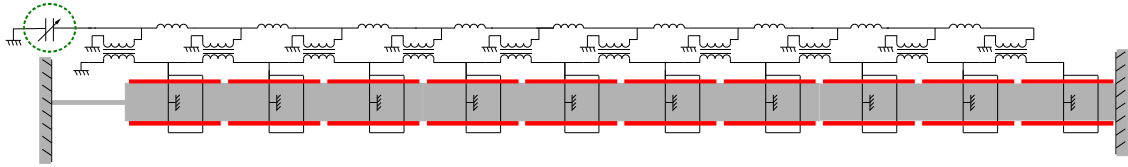
Fig. 2. Electrical analogue of a cantilever beam made of $n = 10$ unit cells.

Fig. 3. Beam coupled to its electrical analogue through an array of piezoelectric patches.

the present case, however, one has to take into account the clamping through the thin lamina. In the linear regime, the lamina can be modeled by a spring of stiffness k^{end} . So, its analogue is a capacitor to be placed at the end of the electrical network, as shown in Fig. 3. The next question is to determine the value of the capacitance that ensures the analogy with the mechanical stiffness. First considering a purely mechanical case, identical eigenfrequencies are obtained for two structures having the same nondimensionalized dynamic equations. In the present example, a nondimensionalized parameter involving the end stiffness is $a^2 k^{\text{end}} / k_\theta$. The analogous electrical parameter is $\hat{a}^2 C / C^{\text{end}}$ because of the equivalence between a capacitance and a compliance and between a lever and a transformer. A relation linking the end capacitance to its analogous linear stiffness is thus given by

$$C^{\text{end}} = \frac{k_\theta}{k^{\text{end}}} \frac{\hat{a}^2}{a^2} C. \quad (11)$$

This end capacitance stiffens the electrical network in a similar way that the lamina stiffens the mechanical structure. As shown by the following numerical results, the additional capacitance in Eq. (11) ensures the frequency condition in Eq. (4) so as to generate a real analogy in the electrical domain.

2.4. Linear model for the electromechanical structure

As seen in Fig. 3, the considered beam is covered with a piezoelectric network in such a way that the electromechanical system consists of a periodic layout of electromechanical unit cells coupling mechanical and electrical degrees of freedom. Focusing on a single unit cell of the one-dimensional waveguide in Fig. 4, the mechanical displacement vector is denoted $\mathbf{q}_m = [\mathbf{q}_{mL} \quad \mathbf{q}_{mR}]^T$ and the electrical charge displacement vector is $\mathbf{q}_e = [\mathbf{q}_{eL} \quad \mathbf{q}_{eR}]^T$, where the letters 'L' and 'R' refer the left and right sides of the unit cell. Similarly, a force vector $\mathbf{F}_m = [\mathbf{F}_{mL} \quad \mathbf{F}_{mR}]^T$ is defined together with a vector containing the electrical voltages on both sides of the unit cell, $\mathbf{F}_e = [\mathbf{F}_{eL} \quad \mathbf{F}_{eR}]^T$. Then, as detailed in [25], the mechanical and electrical degrees of freedom can be combined thanks to the following matrix formulation :

$$\begin{bmatrix} \mathbf{M}_m & \mathbf{0} \\ \mathbf{0} & \mathbf{M}_e \end{bmatrix} \begin{bmatrix} \dot{\mathbf{q}}_m \\ \dot{\mathbf{q}}_e \end{bmatrix} + \begin{bmatrix} \mathbf{C}_m & \mathbf{0} \\ \mathbf{0} & \mathbf{C}_e \end{bmatrix} \begin{bmatrix} \dot{\mathbf{q}}_m \\ \dot{\mathbf{q}}_e \end{bmatrix} + \begin{bmatrix} \mathbf{K}_m + \frac{1}{C} \mathbf{K}_c \mathbf{K}_c^T & \frac{1}{C} \mathbf{K}_c \mathbf{S}^T \\ \frac{1}{C} \mathbf{S} \mathbf{K}_c^T & \mathbf{K}_e \end{bmatrix} \begin{bmatrix} \mathbf{q}_m \\ \mathbf{q}_e \end{bmatrix} = \begin{bmatrix} \mathbf{F}_m \\ \mathbf{F}_e \end{bmatrix}, \quad (12)$$

where $\dot{\mathbf{q}}$ and $\ddot{\mathbf{q}}$ are the first and second time derivatives of the displacement vectors \mathbf{q} , the matrices \mathbf{K}_m , \mathbf{C}_m and \mathbf{M}_m are the mechanical stiffness, damping and mass matrices, respectively, whereas \mathbf{K}_e , \mathbf{C}_e and \mathbf{M}_e are their electrical analogues. The constant

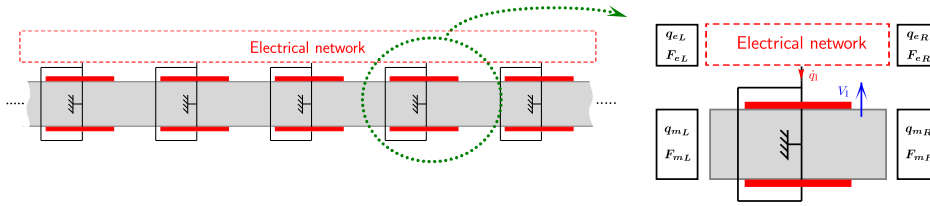


Fig. 4. Interconnected array of piezoelectric patches and corresponding unit cell with left and right electromechanical degrees of freedom [25].

Table 2

Values of the electrical components for the model with $n = 100$ unit cells.

Transformer ratio	$\hat{a} = 2$
Piezoelectric capacitance	$C = 5.08 \text{ nF}$
Inductance	$L = 0.247 \text{ mH}$
Resistance (in inductor)	$R_L = 8.21 \text{ m}\Omega$
Resistance (in capacitor)	$R_C = 18.2 \text{ k}\Omega$
Resistance (in transformer)	$R_T = 76.1 \text{ }\Omega$
End capacitance	$C^{\text{end}} = 14.5 \text{ mF}$

C is the capacitance of the unit cell at zero mechanical displacement, \mathbf{K}_e is a coupling vector and \mathbf{S} is a matrix that only depends on the internal connections of the electrical network:

$$\mathbf{q}_l = \mathbf{S}^T \mathbf{q}_e, \quad (13)$$

where q_l is the electrical charge flowing through the piezoelectric patches as seen in Fig. 4. With the proposed formulation, the coupled problem is organized like any mechanical problem involving mass, damping and stiffness symmetric matrices. The only difference is that the displacement and force vectors contain both mechanical and electrical contributions.

First focusing on the mechanical degrees of freedom, Appendix provides all the details required to build the matrices \mathbf{M}_m , \mathbf{K}_m and \mathbf{K}_e in Eq. (12) for the case of homogenized piezoelectric beam unit cells. The constants used for the numerical calculations are given in Table 1. No mechanical damping is considered ($\mathbf{C}_m = \mathbf{0}$) and 100 elements are employed to discretize the whole cantilever beam. This is largely sufficient because the focus is on the first three modes of the beam. Concerning the electrical matrices in Eq. (12), the topology of the electrical network has to be considered. The purely electrical unit cell in Fig. 1 leads to the electrical charge displacement and voltage vectors:

$$\mathbf{q}_e = \begin{bmatrix} q_{wL} \\ q_{\theta L} \\ q_{wR} \\ q_{\theta R} \end{bmatrix} \quad \text{and} \quad \mathbf{F}_e = \begin{bmatrix} V_{wL} \\ V_{\theta L} \\ -V_{wR} \\ -V_{\theta R} \end{bmatrix}, \quad (14)$$

where the electrical charge displacements q_w and q_θ are the analogues of the linear and angular mechanical displacements W and θ , whereas the opposite of the voltage contributions V_w and V_θ are the analogues of the shear force and bending moment, respectively [10]. The set of discrete equations obtained from Fig. 1 gives the electrical matrices \mathbf{S} , \mathbf{M}_e , \mathbf{C}_e and \mathbf{K}_e that are detailed in Appendix. The numerical values used for the electrical components are given in Table 2. The constant \hat{a} depends on the transformer ratio that is selected for the realization of the electrical network, and the inductance L can then be tuned from Eq. (10).

2.5. Piezoelectric coupling factors

The stiffness of the thin lamina k^{end} and its analogous capacitance C^{end} can be added to the model by introducing diagonal terms in the final stiffness matrix at the positions of the corresponding two degrees of freedom. In the end, analogous boundary conditions are applied to the mechanical and electrical degrees of freedom: W , θ , q_w , q_θ are all fixed at the clamped end, whereas the other degrees of freedom are free from external loads. The resulting FE model of the $n = 100$ electromechanical unit cells is only made of 400 degrees of freedom which allows fast and sufficiently accurate computing of the low-frequency dynamics.

To compute the short- and open-circuit eigenfrequencies of the electromechanical model, L is set to 0 or to a very large value compared to the nominal one, respectively. This means that, if there are additional capacitors in the electrical network, the so-called short-circuit eigenfrequency is not necessarily the same as when short-circuiting all the piezoelectric patches. The first short-circuit eigenfrequency with an infinite end-capacitance is employed to update k^{end} from available experimental data [14]. The analogous capacitance C^{end} can then be calculated from Eq. (11). The eigenfrequencies of the first three modes are given in Table 3 together with the corresponding coupling factors. The first coupling factor is smaller because of the influence of both the additional capacitance and the end stiffness due to the lamina. While having an important contribution in the modal stiffness of the first mode, the lamina does not participate to the piezoelectric coupling because the patches are only placed along the main beam. Conversely, the lamina and the additional capacitance do not have a strong influence on the higher modes so that the coupling factors are very similar to those obtained with a cantilever beam.

Table 3
Eigenfrequencies and coupling factors for the first three modes of the ideal beam.

	f_s (Hz)	f_o (Hz)	k_c
Mode 1	29.72	30.03	0.144
Mode 2	154.14	157.37	0.206
Mode 3	429.27	438.43	0.208

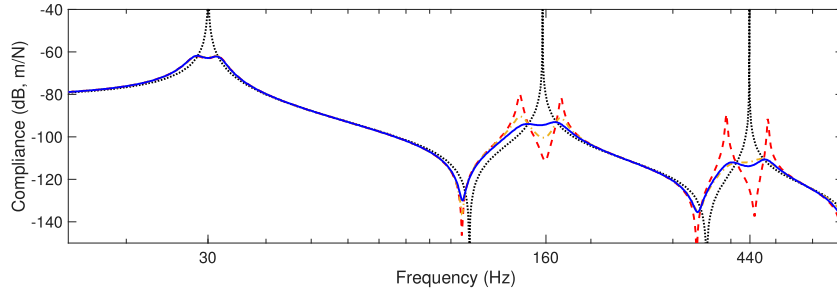


Fig. 5. Simulated FRF with open-circuited patches (···) and after coupling to the piezoelectric network with R_L only (---), with R_L and R_C (-.-.-) and with R_T only (—).

2.6. Optimal resistance for multimodal damping

Although the tuning of the network inductance from Eq. (10) ensures similar natural frequencies in the mechanical and electrical domains, damping is also required in the electrical network. Because it corresponds to what is usually observed in practice, the first case considered is a resistance in series with the inductance, i.e., $R_L \neq 0$ and $R_C = R_T = 0$, see Fig. 1. According to Eq. (5), the optimal damping for the first mode requires

$$R_L = \sqrt{\frac{3}{2}} k_{c1} \omega_{o1} L. \quad (15)$$

The FRF at the end of the beam in Fig. 5 depicts that approximately equal peaks are obtained for the first mode. However, the second and third modes require more damping, as evidenced by the dependence on ω_{o1} in Eq. (15).

When a resistance is in series with the capacitance, i.e., $R_C \neq 0$ and $R_L = R_T = 0$, the electrical quality factor is $1/(\omega C R_C)$ and the optimal resistance is

$$R_C = \sqrt{\frac{3}{2}} \frac{k_c}{\omega_o C}. \quad (16)$$

The inverse dependence on ω_o means that lower-frequency modes require a greater resistance value. A good trade-off would thus tune R_L on the first mode with Eq. (15) and R_C on the third mode with Eq. (16). Fig. 5 shows that the first and third modes are now well damped, but the second mode is still underdamped.

Another option is to introduce damping through the resistance in series with the transformer winding, i.e., R_T in Fig. 1, as considered by Porfiri et al. [9]. In this study, they showed that the optimal resistance for a simply supported beam,

$$R_T^{SS} = \sqrt{2} e_\theta \frac{\hat{a}}{C} \sqrt{\frac{L}{k_\theta^D}}, \quad (17)$$

does no longer depend on frequency (see Appendix for the definition of e_θ and k_θ^D). Even if there is no analytical formulation available for a cantilever beam, the numerical results in Fig. 5 show that a resistance $R_T \approx 0.6 R_T^{SS}$ is close to the optimum. We note that it remains a theoretical solution as the resistance in series with the inductance cannot be neglected in practice.

In summary, the results in Fig. 5 confirm that an analogous electrical network can effectively provide effective multimodal vibration mitigation.

3. Piezoelectric vibration mitigation of a nonlinear structure

3.1. Single mode damping with a nonlinear piezoelectric tuned vibration absorber

Resonant piezoelectric shunting ensures that the electrical resonance at angular frequency $1/\sqrt{L^* C^*}$ matches the open-circuit natural frequency ω_o . Because it alters this latter frequency, mechanical nonlinearity results in the detuning of the piezoelectric shunt, which eventually alters damping performance [14].

To overcome the adverse effect of nonlinearities, as opposed to piezoelectric energy sinks [26,27], a solution is to introduce subtle nonlinearities in the electrical circuit according to a principle of similarity, i.e., the added nonlinearity should possess the

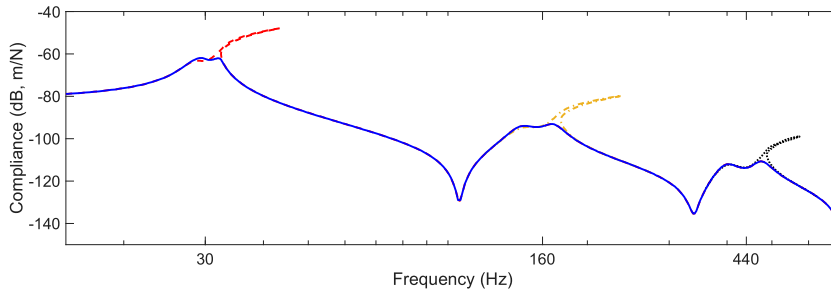


Fig. 6. Simulated FRF with the optimal resistance R_T and the nonlinear mechanical stiffness but no nonlinear capacitance for $F = 0.67$ N from 15 Hz to 700 Hz (—), for $F = 130$ N around 160 Hz (— · —) and for $F = 2400$ N around 440 Hz (···) and with the nonlinear capacitance for $F = 0.67$ N from 15 Hz to 700 Hz (—).

same mathematical form as that in the mechanical system [17]. This tuning strategy was validated experimentally on a single mode thanks to a fully passive nonlinear inductor exploiting the saturation in the magnetic circuit [14]. It was then shown in [16] that similar results can be obtained with a digital impedance able to synthesize an adequate nonlinear capacitance. For example, if the nonlinear mechanical force is a cubic function of the displacement u , $f_{NL} = k_{NL}u^3$, the required additional voltage in the shunt should be a cubic function of the electrical charge q [13,14]:

$$v_{NL} = \frac{1}{C_{NL}} q^3 \quad \text{with} \quad \frac{1}{C_{NL}} = 2 \left(\frac{L_i^*}{m_i^*} \right)^2 k_{NL}. \quad (18)$$

Adding this nonlinear capacitance in series with the inductor maintains an equal-peak condition over a much broader range of excitation amplitudes.

3.2. Extension to mitigation of multiple nonlinear resonances

Targeting now the mitigation of multiple nonlinear resonances, the objective is to find the adequate nonlinearity to be introduced in the electrical network. For a cubic nonlinear stiffness, Eq. (18) gives

$$\frac{1}{C_{NLi}} = 2 \left(\frac{L_i^*}{m_i^*} \right)^2 k_{NL}, \quad (19)$$

where L_i^* is the modal inductance of the network for electrical mode i . Because there is a priori no specific relation between the modal inductance L_i^* and the modal mass m_i^* , the optimal electrical nonlinearity necessarily depends on mode number, as seen in Eq. (19).

To address this issue, our objective is to develop a nonlinear analogous electrical network which combines the modal analogy used for linear multimodal damping and the principle of similarity used for nonlinear damping. The modal analogy implies that the mechanical and electrical systems have the same natural frequencies $\omega_{oi} = \sqrt{k_i^*/m_i^*} = 1/\sqrt{L_i^*C_i^*}$ and the same mode shapes. Identical eigenvalue problems for the two systems means that the modal “mass ratio” $r = L_i^*/m_i^*$ is the same for all modes. As a consequence, the optimal value for the nonlinear capacitance

$$\frac{1}{C_{NL}} = 2r^2 k_{NL}, \quad (20)$$

becomes independent of the mode number.

For the beam example, the load applied by the lamina can be modeled by a nonlinear force $f = k_{NL}^{\text{end}}u + k_{NL}u^3$ where u is the displacement at the end of the main beam [14]. The voltage $v = \frac{1}{C_{\text{end}}}q + \frac{1}{C_{NL}}q^3$ is thus required in the end capacitor which is the analogue of the thin lamina. For the beam, the mass ratio is $r = L/m$, where m is the mass of the unit cell and L is the corresponding inductance in the network. The numerical value for the nonlinear capacitance is then obtained from Eq. (20):

$$\frac{1}{C_{NL}} = 2 \left(\frac{L}{m} \right)^2 k_{NL}. \quad (21)$$

3.3. Numerical validation of the nonlinear analogous electrical network

A nonlinearity $k_{NL} = 2.5 \times 10^9 \text{ N m}^{-3}$ is introduced in the linear model developed in Section 2 to account for the geometrically nonlinear effect of the thin lamina. The nonlinear frequency responses in Fig. 6 were obtained using numerical continuation and the harmonic balance method with 5 harmonics. As shown in Fig. 7, above a forcing amplitude $F = 0.67$ N, vibration mitigation of the first mode is severely affected by the mechanical nonlinearity. The same distortions appear for the second and third modes

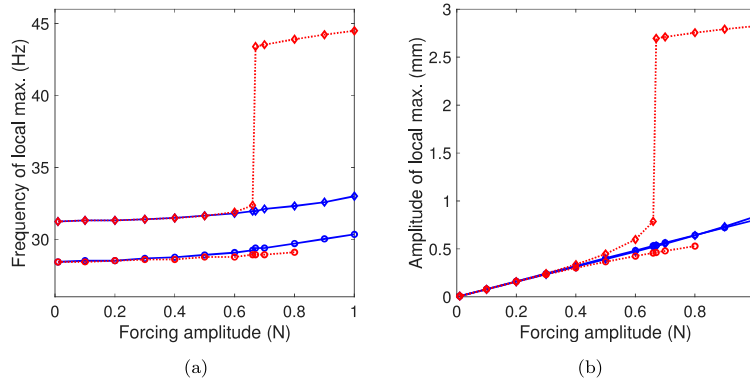


Fig. 7. Frequency (a) and amplitude (b) of the local maxima around mode 1 as a function of the forcing amplitude without nonlinear capacitor (---) and with a nonlinear capacitor (—). Both diamond and circle markers appear when the considered frequency response features two local maxima.

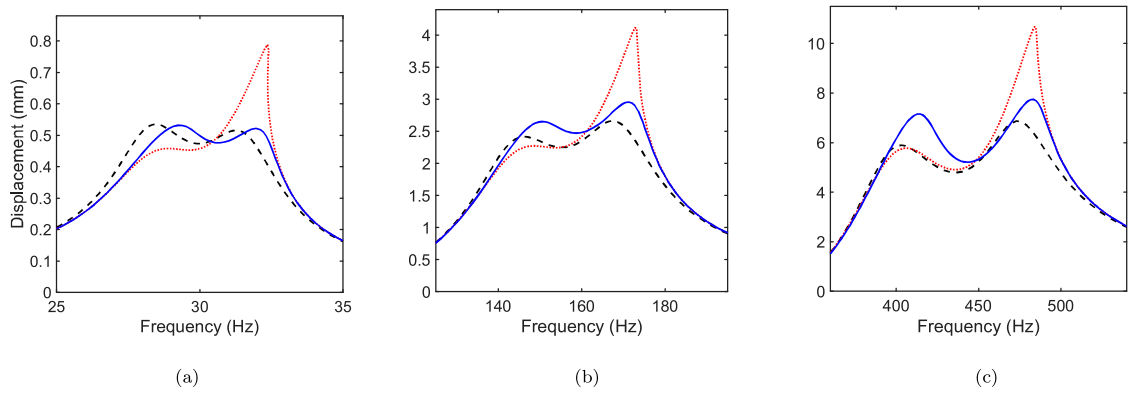


Fig. 8. Simulated responses for the first three modes of the nonlinear beam connected to a network without nonlinear capacitance (---), with optimal nonlinear capacitance (—) and for a linear beam connected to a linear network (---): (a) mode 1 for $F = 0.66$ N, (b) mode 2 for $F = 120$ N, (c) mode 3 for $F = 2350$ N.

for $F = 130$ N and 2400 N, respectively.¹ According to Eq. (21), whose constants are obtained from Tables 1 and 2, a nonlinear capacitor $1/C_{NL} = 1.63 \times 10^6$ V C⁻³ is introduced in the electrical circuit. Figs. 6 and 7 evidence that the vibration amplitudes are maintained at levels similar to those obtained in the purely linear case in Fig. 5.

Fig. 8 offers a closer look around the three modes for slightly lower forcing amplitudes, i.e., for amplitudes just below the merging of the right resonance peak with a detached resonance curve when no nonlinearity is introduced in the electrical network [28]. It is clear that the nonlinear network connected to the nonlinear beam has a behavior very close to the linear network connected to the linear beam, hence demonstrating the effectiveness of the concept.

The evolution of the frequency response around the first mode for different values of the nonlinear capacitance and of the resistance is displayed in Fig. 9. Fig. 9(a) confirms that the tuning rule (21) provides the optimal value of the electrical nonlinearity in terms of the H_∞ norm. However, Figs. 9(b–c) shows that Eq. (21) requires appropriate electrical damping. Specifically, the damping in the electrical analogue needs to be as close as possible to the values given in Eq. (5).

4. Experimental validation with the piezoelectric analogue twin

4.1. Piezoelectric beam

The experimental setup in Fig. 10 corresponds to the beam previously described (Table 1). Twenty piezoelectric stacks with two layers were glued on each side of the beam. The beam end was excited with an electrodynamic shaker whereas an impedance head measured the input force and the acceleration. A rational fraction polynomial (RFP) method was used to extract the experimental natural frequencies and the modal damping ratios of the short-circuit and open-circuit FRFs.

Nelder–Mead simplex optimization algorithm was used to update the numerical model from the available experimental data. The objective function is the norm of the vector including the errors on the first and second short-circuit eigenfrequencies as well

¹ Note that those latter force levels are impractical for the experimental demonstration discussed later.

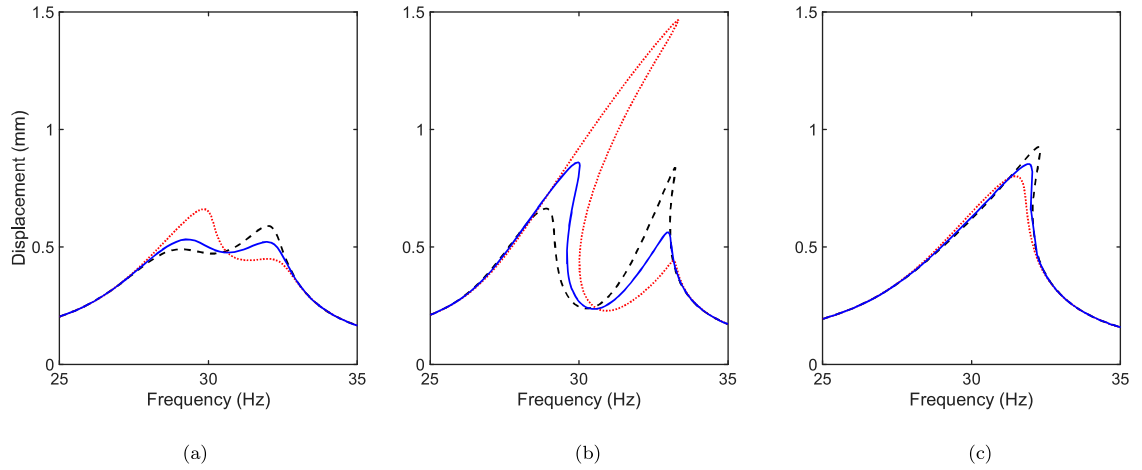


Fig. 9. Simulated nonlinear responses around the mode 1 for $F = 0.66$ N with the nominal nonlinear capacitance (—), with twice the nonlinear capacitance (\cdots) and with half of the nonlinear capacitance (-- --): (a) nominal resistance ($R_T = 0.6 R_T^{\text{SS}}$), (b) underdamped ($R_T = 0.3 R_T^{\text{SS}}$), (c) overdamped ($R_T = R_T^{\text{SS}}$).

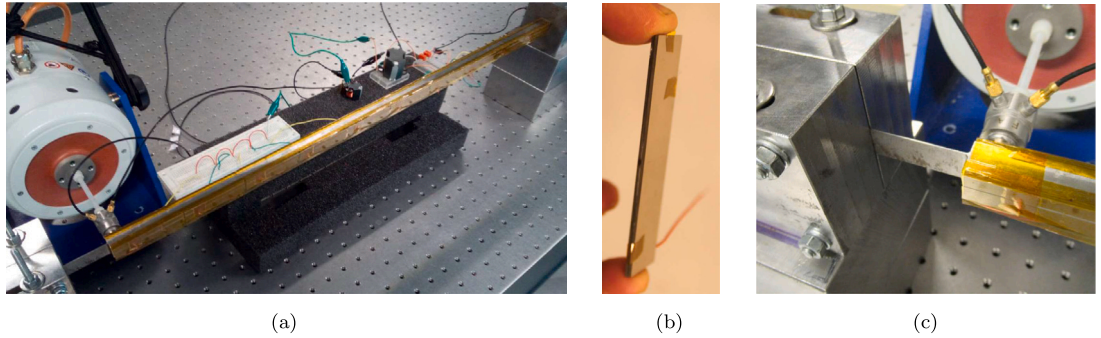


Fig. 10. Experimental setup : (a) cantilever piezoelectric beam with the thin lamina at its left end [14], (b) one of the 2-layer piezoelectric stacks, (c) close-up of the thin lamina and of the impedance head.

Table 4

Updated parameters and correction factors when compared to the numerical model developed in the previous section.

	Initial	Updated	Correction factor
YI (N m ²)	896	789	0.88
k^{end} (N/m)	3810	4789	1.26
e_θ (N m/kV)	5.30	4.19	0.79

Table 5

Short-circuit eigenfrequencies, modal damping ratios and coupling factors of the piezoelectric beam (experimental data and updated numerical model).

	Exp. f_s	Num. f_s	Err. f_s	Exp. ξ_s	Exp. k_c	Num. k_c	Err. k_c
Mode 1	29.54	29.54	0.0%	0.25%	0.137	0.137	0.0%
Mode 2	144.96	144.96	0.0%	0.20%	0.158	0.171	8.3%
Mode 3	397.28	402.93	1.4%	0.48%	0.163	0.169	3.8%

as the first modal coupling factor. The updating parameters are the flexural rigidity YI , the stiffness of the thin lamina k^{end} and the piezoelectric coupling coefficient e_θ . The clamped boundary condition is considered perfect during the optimization because it was observed that it did not strongly influence the results compared to the loss of flexural rigidity. The initial and updated values are listed in Table 4.

We remark that a 12% decrease of the homogenized bending stiffness is required to match the experimental results. This is partly due to the fact that the considered homogenized unit cells do not precisely model the 3D effects around the strong steps induced by the piezoelectric patches (almost 30% increase of the beam thickness). Another reason is that the layers of the home-made

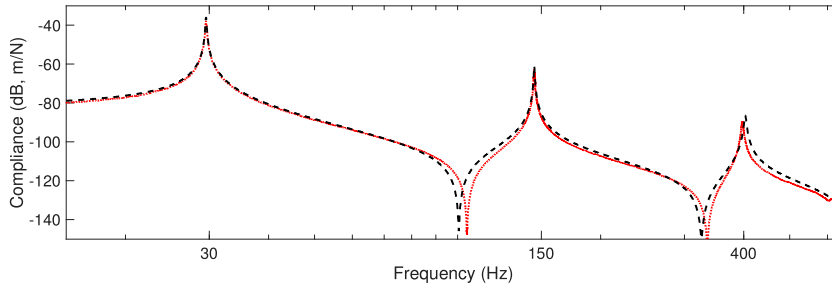


Fig. 11. Experimental (---) and simulated (---) short-circuit FRFs of the piezoelectric beam.

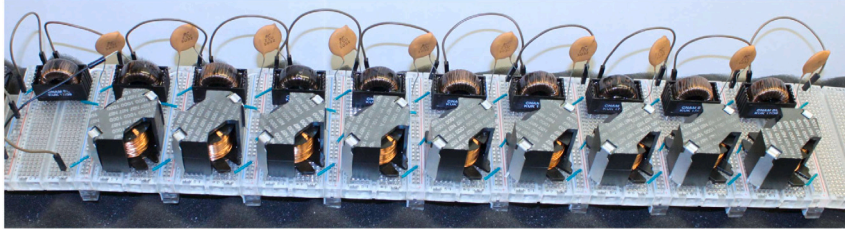


Fig. 12. Electrical analogue of the cantilever beam with passive inductors, transformers and capacitors.

Table 6

Natural frequencies and damping ratios of the electrical network (experimental data and updated numerical model).

	Exp. f_e	Num. f_e	Err. f_e	Exp. ξ_e	Num. ξ_e	Err. ξ_e
Mode 1	30.49	30.49	0.0%	8.15%	8.15%	0.0%
Mode 2	153.78	151.92	1.2%	5.74%	5.74%	0.0%
Mode 3	420.25	414.22	1.4%	8.58%	8.71%	1.5%

piezoelectric stacks are not perfectly glued together. Both reasons also probably explain the decrease in the global piezoelectric coupling coefficient.

The short-circuit natural frequencies, modal damping ratios and coupling factors of the updated model are compared to the experimental values in Table 5. The errors on three quantities are identically zero, because there were three updating parameters. The other errors stay within reasonable limits. Note that the piezoelectric coupling factors cannot be directly compared to those in Table 3 that are calculated with an end capacitance in the network. However, they all remain above 10% which can be qualified as a good piezoelectric coupling for laboratory experiments. The good correlation between experiments and simulations over the frequency range of interest is confirmed in Fig. 11 where modal damping was added to the numerical model according to the experimental damping ratios in Table 5.

4.2. Development of the multi-resonant electrical network

Assembling the analogous network in Fig. 3 requires nine inductors, ten transformers and one capacitor. The transformers feature a ratio $\hat{a} = 2$ and a winding capacitance around 2 nF [10]. As the piezoelectric capacitance was evaluated to 50.8 nF, the total capacitance is $C = 52.8$ nF. Eqs. (10) and (11) were used to calculate the required electrical components. Eventually, the target values for the inductance and end capacitance are $L = 277$ mH and $C^{\text{end}} = 104$ μ F.

The magnetic components were specifically designed for piezoelectric damping applications. For the inductors, RM14 magnetic cores of permeance 1000 nH were wound with 530 turns of copper wire of 0.4 mm diameter. For the transformers, we used the same ungapped nanocrystalline toroids as the ones in [11]. The presence of the thin lamina was implemented in the electrical domain by the addition of a bipolar electrolytic capacitor of value $C^{\text{end}} = 103$ μ F. To validate the electrical dynamics, the ten piezoelectric patches were replaced by 47.2 nF ceramic capacitors. The resulting passive network is shown in Fig. 12.

To validate the sought modal analogy, an impedance meter measured the admittance at the end of the network, as shown in Fig. 13. Considering an infinite end capacitance, i.e., a short circuit, the distributions of the electrical current in Fig. 14 are plotted at frequencies corresponding to the first three maxima of the admittance. It is seen that the distributions are similar to the mode shapes of a clamped beam, which confirms that the electrical network has an adequate spatial behavior. To validate its frequency behavior, the infinite capacitance was replaced by the appropriate end capacitance. The identified natural frequencies and modal damping ratios are listed in Table 6. The end capacitance induces a first resonance around 30 Hz, as required by the mechanical structure.

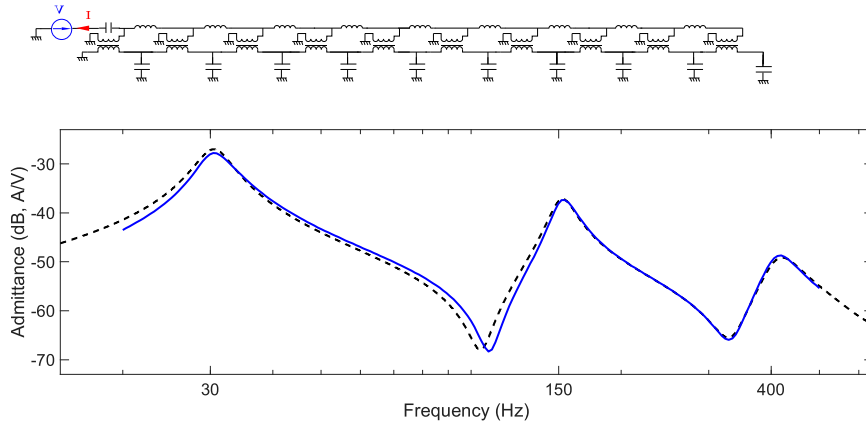


Fig. 13. Experimental (—) and simulated (---) FRFs of the electrical network.

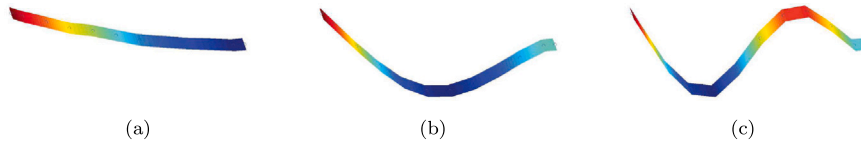


Fig. 14. Experimental distributions of the electrical current: (a) mode 1, (b) mode 2 and (c) mode 3.

Table 7
Parameters of the optimal and actual electrical networks.

	L (mH)	R_L (Ω)	R_C (Ω)	R_T (Ω)	ξ_{e1} (%)	ξ_{e2} (%)	ξ_{e3} (%)	C^{end} (μ F)
Optimal	277	0	0	659	6.91	10.28	8.82	104
Actual	277	6.82	1000	137	8.15	5.74	8.58	103

Because direct measurements on the isolated electrical components have to be performed at a specific frequency and amplitude, we preferred to resort to model updating to take into account the real electrical dynamics including the potential effect of unmodeled parasitic elements. For example, the copper wire resistance in the inductors and transformers was added to the model because of its strong influence on the electrical quality factors. This is also true for the additional resistors in series with the capacitors. However, the magnetizing inductance of the transformers [10] was not taken into account so it may have a slight influence on the equivalent inductance obtained from the first natural frequency. The model of the electrical network was thus updated using parameters for the inductance L , its series resistance R_L and the resistance of the transformer R_T . The objective function is the norm of the vector including the error on the first natural frequency as well as the errors on the first and second damping ratios, as illustrated in Table 6. The electrical parameters resulting from this model updating are given in Table 7. Figure 13 shows the good agreement between the experimental results and the numerical simulations computed from the updated model of the electrical circuit.

The optimal modal damping ratios listed in Table 7 were obtained from Eq. (4). Note that the first damping ratio of the actual network is slightly above its optimal value, because the resistance R_L of the inductors could not be reduced to a sufficiently low value with the chosen magnetic components. Thanks to the addition of resistors $R_C = 1$ k Ω in series with the capacitors, the third damping ratio is very close to its optimum. The second damping ratio is deliberately left below its optimal value to avoid the deterioration of the other damping ratios.

4.3. Linear multimodal damping

The full setup can be seen in Fig. 15 where the electrical network in Fig. 12 is coupled with the beam through the array of piezoelectric patches. The comparison between the FRFs with open-circuited patches and with the electrical network in Fig. 16 evidences that effective multimodal damping is achieved for the first three modes of the beam. The vibration amplitude is reduced by factors of 14, 32 and 9 for modes 1, 2 and 3, respectively. As anticipated in Table 7, the first mode is, however, overdamped. A very good agreement between the experimental and numerical FRFs can also be noticed. Note that the piezoelectric capacitance is considered constant in the present study although experiments in [14] suggest that the introduction of a linear variation of the capacitance with respect to the voltage amplitude may improve the model.

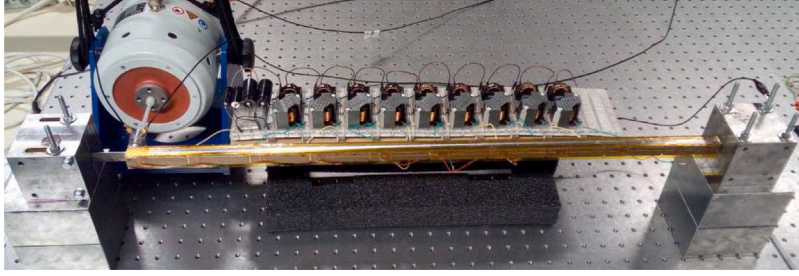


Fig. 15. The piezoelectric beam coupled to its analogous electrical network.

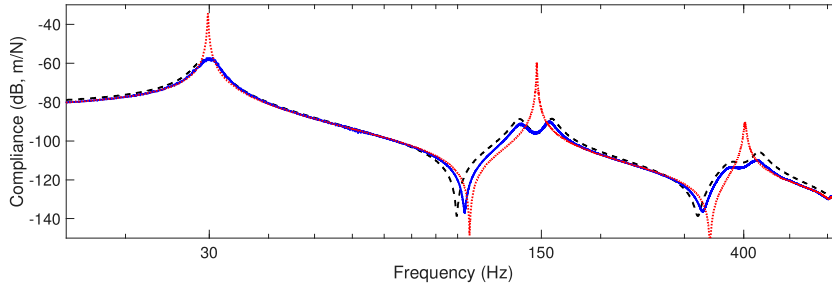


Fig. 16. FRFs with open-circuited patches (---) and with the analogous electrical network (model: -- and experiment: —).

4.4. Nonlinearity in the analogous electrical network

To guarantee satisfactory performance when the mechanical nonlinearity induced by the thin lamina is activated at greater forcing levels, a nonlinear capacitor satisfying Eq. (18) is to be incorporated in the electrical network. The first-harmonic approximation is $V_{NL} = \frac{3}{4C_{NL}}Q^3$, where V_{NL} is the amplitude of the nonlinear voltage contribution and Q is the amplitude of the electrical charge. If this nonlinear component is in series with the linear capacitor C^{end} , the equivalent variable capacitance is defined as

$$C_{NL}^{end}(Q) = \frac{1}{\frac{1}{C^{end}} + \frac{3Q^2}{4C_{NL}}}. \quad (22)$$

We attempted to implement this law using a capacitor excited beyond its nominal voltage range [29,30], i.e., a 100 μ F chip multilayer ceramic capacitor with a 2.5 V maximum voltage for conventional use. To characterize its nonlinear behavior, a 30 Hz harmonic voltage with a variable amplitude from 0 to 22 V was applied to a 100 Ω resistance in series with the capacitor. The time series of the voltage across the nonlinear capacitor v is depicted in Fig. 17(a). Integrating the current \dot{q} flowing through the capacitor gives a way to plot the hysteresis curve q as a function of v , as in Fig. 17(b). This figure displays that the selected ceramic capacitor can exhibit a significant nonlinear behavior.

The equivalent capacitance and resistance values at 30 Hz are defined from

$$v^* = \frac{1}{C_{eq}}q^* + R_{eq}\dot{q}^*, \quad (23)$$

where the time signals filtered with a passband filter between 20 Hz and 40 Hz are

$$v^* = V \cos(\omega t + \delta_v), \quad q^* = Q \sin(\omega t + \delta_q) \quad \text{and} \quad \dot{q}^* = \dot{Q} \cos(\omega t + \delta_q). \quad (24)$$

Consequently,

$$C_{eq} = -\frac{Q}{V} \sin(\delta_v - \delta_q) \quad \text{and} \quad R_{eq} = \frac{V}{\dot{Q}} \cos(\delta_v - \delta_q). \quad (25)$$

The equivalent values were computed by extracting the amplitudes V , Q and \dot{Q} , as well as the phase shifts δ_v and δ_q . The equivalent resistance R_{eq} was found to be negligible with respect to the other dissipative components. The variation of the capacitance as

Table 8
Optimal and actual values for the nonlinear capacitor.

	C^{end} (μF)	$1/C_{\text{NL}}$ (V C^{-3})
Optimal	104	2.05×10^{10}
Actual	105	3.12×10^{10}

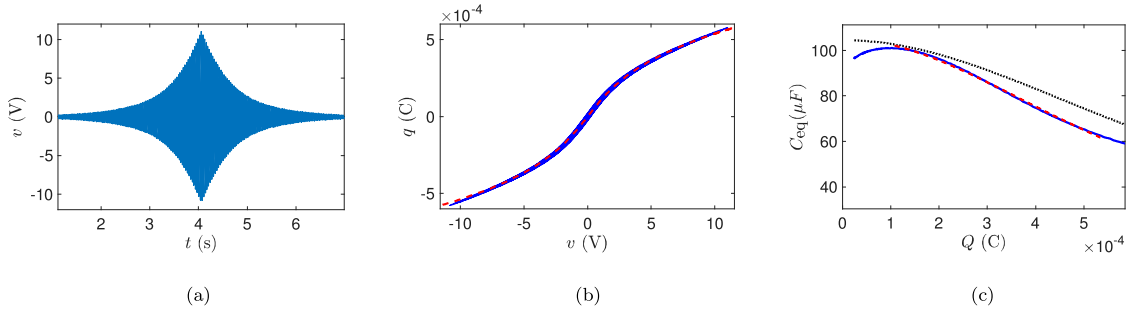


Fig. 17. Measurement of the equivalent capacitance: (a) voltage applied across the capacitor, (b) electrical charge as a function of the voltage (experiment: —, and curve fitting: - -), (c) theoretical nonlinear capacitance (···), equivalent capacitance (experiment: —, and curve fitting: - -).

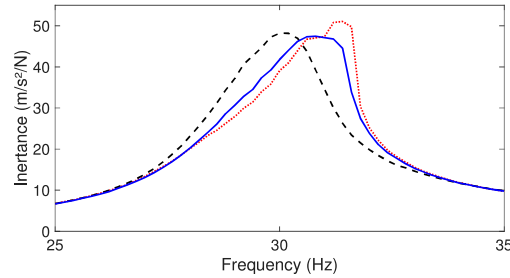


Fig. 18. Experimental FRF around mode 1 with the nonlinear capacitor for $F = 0.2 \text{ N}$ (---) and $F = 0.35 \text{ N}$ (—), and with the linear capacitor for $F = 0.35 \text{ N}$ (···).

a function of the electrical charge amplitude is plotted in Fig. 17(c). For comparison, the figure also displays the theoretical capacitance (22). A curve fitting was applied to extract the approximate end capacitance C^{end} and nonlinear capacitance $1/C_{\text{NL}}$ in Table 8. The curve fitting was performed over a limited range of the electrical charge amplitudes approximated from the linear model for input forces ranging from 0.2 N to 1 N. Comparing the values in Table 8 shows that the nonlinearity of the experimental capacitor is greater than the optimal nonlinearity. However, since the first vibration mode is overdamped, an increase of the electrical nonlinearity can be beneficial for maintaining an adequate tuning in the nonlinear range, as illustrated in Fig. 9(c). The chosen capacitor was thus considered as a sufficiently good candidate for the experimental validation.

4.5. Vibration mitigation with the nonlinear analogous electrical network

Two important limitations arose when carrying out experiments with the nonlinear analogous electrical network. First, as shown in Figs. 8(b–c), activating the nonlinearity for the second and third modes demands forcing amplitudes that are well beyond the capabilities of the electrodynamic shaker. Second, forcing levels above 0.2 N generate an unforeseen magnetic saturation in some of the electrical transformers, leading to a decrease in the magnetizing inductance of the transformers. This means that, even without the nonlinear capacitor, the first resonance exhibits a non-negligible nonlinear behavior, which prevented us from demonstrating the anticipated performance of the network. Fig. 18 actually shows the greatest difference observed between the nonlinear and the supposedly linear networks before entering a fully nonlinear regime with bistable solutions. The experiment with the nonlinear capacitor shows the expected behavior but the unexpected results concern the case with the linear capacitor that should normally demonstrate greater detuning if the electrical resonance were at a constant frequency.

A technical solution could be to manufacture a new series of transformers of slightly larger dimensions. A larger magnetic cross section would increase the saturation limit and thus extend the linear range of the electrical network to greater excitation

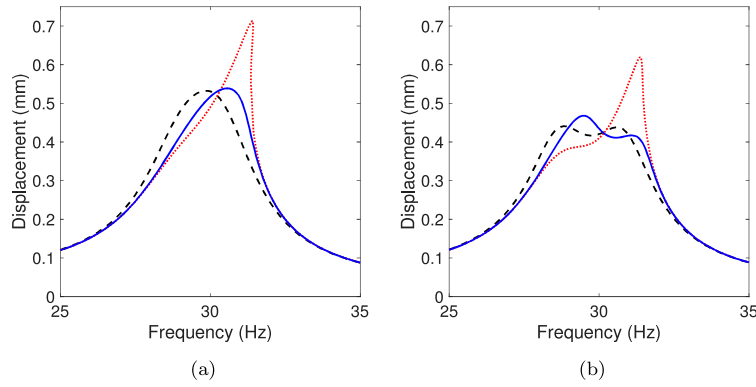


Fig. 19. Realistic simulations using an electromechanical model considering the experimental parameters. Response around mode 1 for $F = 0.4$ N when the nonlinear beam is coupled to the linear (---) or nonlinear (—) electrical networks. Linear beam coupled to the linear network (---). (a) Resistance values in Table 7, (b) 30% decrease of R_L .

levels. However, since the production of a fully new electrical network was not feasible, we propose herein to benefit from the developments in Sections 3 and 4 to carry out realistic simulations in order to, at least partially, validate the nonlinear analogous network. The advantage of such simulations is that the parasitic effect of magnetic saturation in the transformers is obviously not present. Specifically, a nonlinear electromechanical model considering the experimental parameters in Tables 4, 7 and 8 was built.

Fig. 19(a) presents the first resonance at a forcing level of 0.4 N for three different configurations, namely the nonlinear beam coupled to either the linear or the nonlinear network and the linear beam coupled to the linear network. When the linear network is coupled to the nonlinear beam, the mechanical nonlinearity induced by the thin lamina leads to a significant detuning as well as a clear hardening of the resonance peak. The addition of the nonlinear capacitor decreases the amplitude at resonance to a level which is almost identical to that of the linear beam coupled to the linear network, hence confirming that a proper nonlinear capacitor was selected.

Fig. 19(b) gives the results of a simulation for which the first mode is no longer overdamped. To this end, a 30% decrease of the resistance R_L in series with the inductors was considered; this can be envisioned in practice by selecting other magnetic cores for the passive inductors. The benefit of the nonlinear capacitor is again evident. We note that a strict equal peak condition cannot be achieved, because the parameters of the selected nonlinear capacitor deviate away from the optimal parameters in Table 8.

The comparison between cases with and without nonlinear capacitor is shown for different forcing amplitudes in Fig. 20. The electrical parameters used to plot Fig. 19(a) lead to Figs. 20(a) and (c). The jump of the single maxima to greater vibration amplitudes occurs at $F = 0.41$ N with the linear network and at $F = 0.71$ N with the nonlinear capacitor. This limit forcing amplitude was above 1 N with the theoretical model as illustrated in Fig. 7. The main reason for such a decrease is the fact that the resistance is above its optimal value in the realistic simulations that represent the experimental setup. Indeed, with a lower resistance, Figs. 20(b) and (d) show that a behavior close to the one observed in Fig. 7 is retrieved with the appearance of two local maxima. The remaining difference is the unequal amplitude of the two maxima that is again due to the slightly imprecise tuning of the chosen nonlinear capacitor.

5. Conclusions

The objective of this study was to show that multimodal vibration mitigation of nonlinear systems can be achieved with fully passive piezoelectric networks. To this end, we proposed to couple a mechanical structure to its nonlinear electrical analogue, realizing in essence what we call an analogue twin of the mechanical structure.

Linear multi-resonant networks offer vibration mitigation over a wide frequency range. However, the presence of a mechanical nonlinearity can substantially increase the vibration amplitudes because of the increasing detuning between the mechanical and electrical resonances. The numerical simulations carried out in this paper evidenced that adding to the network an electrical nonlinearity similar to the mechanical one (both in mathematical form and spatial positioning) leads to effective broadband attenuation, similar to that obtained in the purely linear case. An experimental analogous network was also built and led to the selection of an adequate electrical nonlinearity. Magnetic saturation in the transformers did not allow an explicit experimental validation with the proposed setup but simulations with realistic parameters approved the choice of the considered nonlinear capacitor.

An interesting perspective of this research is to realize the required electrical nonlinearities (or even parts of the linear network) with digital components, leading to a hybrid, semi-passive piezoelectric network that can adapt itself to, e.g., changing environmental conditions.

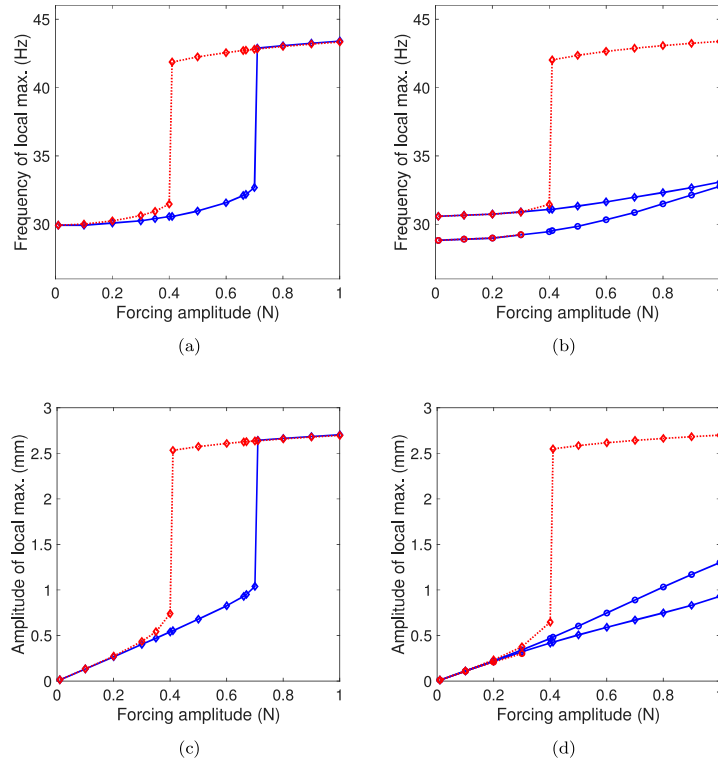


Fig. 20. Characteristics of the local maxima around mode 1 as functions of the forcing amplitude without nonlinear capacitor (...) and with a nonlinear capacitor (—): (a) frequency and (c) amplitude of the single local maximum when considering the resistance values in Table 7, (b) frequency and (d) amplitude of the local maxima with a 30% decrease of R_L . Both diamond and circle markers appear when the considered frequency response features two local maxima.

CRediT authorship contribution statement

Boris Lossouarn: Conceptualization, Methodology, Formal analysis, Investigation, Writing - original draft, Writing - review & editing. **Gaetan Kerschen:** Conceptualization, Writing - review & editing. **Jean-François Deü:** Conceptualization, Writing - review & editing.

Declaration of competing interest

The authors declare that they have no known competing financial interests or personal relationships that could have appeared to influence the work reported in this paper.

Appendix

The objective of this Appendix is to provide the technical details required to build the piezoelectric beam model. While the following elements have already been introduced in previous papers [10,25], they are here summarized in order to offer to any interested reader the possibility of a full implementation of the proposed electromechanical model.

For an Euler–Bernoulli beam, the finite element model based on cubic shape functions for the transverse displacement involves the stiffness matrix

$$\mathbf{K}_m = \frac{YI}{a^3} \begin{bmatrix} 12 & 6a & -12 & 6a \\ 6a & 4a^2 & -6a & 2a^2 \\ -12 & -6a & 12 & -6a \\ 6a & 2a^2 & -6a & 4a^2 \end{bmatrix}, \quad (\text{A.1})$$

where Y is the Young's modulus and I is the second moment of area of the beam element of length a . Moreover, the mass matrix is

$$\mathbf{M}_m = \frac{\rho S a}{420} \begin{bmatrix} 156 & 22a & 54 & -13a \\ 22a & 4a^2 & 13a & -3a^2 \\ 54 & 13a & 156 & -22a \\ -13a & -3a^2 & -22a & 4a^2 \end{bmatrix}, \quad (\text{A.2})$$

where ρ is the density and S the cross-sectional area of the beam. Considering that each element is a laminated structure, homogenized quantities are used in the finite element model. The homogenized flexural rigidity YI of the piezoelectric bimorph is obtained from the bending compliance of the unit cell,

$$\frac{a}{YI} = \frac{l_p}{Y_b I_b + 2Y_p^E I_p} + \frac{a - l_p}{Y_b I_b}, \quad (\text{A.3})$$

and the mass is $\rho S a = \rho_b h_b b a + 2\rho_p h_p b l_p$, where the constants are given in Table 1.

The mechanical displacement vector for the homogenized segment of Euler-Bernoulli beam is $\mathbf{q}_m = [W_L \ \theta_L \ W_R \ \theta_R]^T$. Because the poling direction of the piezoelectric patches have been chosen so that coupling occurs for bending motion, the coupling vector is defined as

$$\mathbf{K}_c = e_\theta [0 \ 1 \ 0 \ -1]^T, \quad (\text{A.4})$$

where

$$e_\theta = \sqrt{C(k_\theta^D - k_\theta^E)} \quad (\text{A.5})$$

is the piezoelectric coupling coefficient related to bending motion [10]. The constant $k_\theta^E = YI/a$ corresponds to the bending stiffness of a unit cell in short circuit, which can be obtained directly from Eq. (A.3). On the other hand, k_θ^D is the open-circuited bending stiffness that is calculated from the same equation after replacing the Young's modulus at zero electric field, Y_p^E , by the Young's modulus at zero electric charge displacement,

$$Y_p^D = \frac{1}{\frac{1}{Y_p^E} - \frac{d_{31}^2}{\epsilon_{33}^\sigma}}. \quad (\text{A.6})$$

In Eq. (A.5) also appears the constant C that represents the piezoelectric capacitance of a unit cell when the mechanical displacements are blocked ($\mathbf{q}_m = \mathbf{0}$). The blocked capacitance of a single piezoelectric patch is calculated from

$$\hat{C} = \epsilon_{33}^\epsilon \frac{b l_p}{h_p}, \quad (\text{A.7})$$

where ϵ_{33}^ϵ is the equivalent permittivity of the piezoelectric material when no bending of the unit cell. While a precise estimation of this permittivity requires 3D calculations [31], it can still be approximated from a 1D model with

$$\epsilon_{33}^\epsilon = \epsilon_{33}^\sigma - Y_p^E d_{31}^2. \quad (\text{A.8})$$

In the present paper, as described in the experimental section, each unit cell of the considered setup involves four piezoelectric patches of thickness $\hat{h}_p = h_p/2 = 1$ mm. Each pair of patches makes a two-layer stack of thickness h_p and the two stacks are connected in parallel. The blocked capacitance of a single unit cell is thus $C = 4\hat{C}$.

Concerning the electrical network, Eq. (13) and the relation between the external electric charge displacements and the charge on the electrodes of the piezoelectric patches $q_L = q_{\theta L} - q_{\theta R}$ gives

$$\mathbf{S} = [0 \ 1 \ 0 \ -1]^T. \quad (\text{A.9})$$

Furthermore, symbolic computations based on the discrete equations describing the unit cell in Fig. 1 give the mass, damping and stiffness matrices for the electrical network:

$$\mathbf{M}_e = \frac{L}{2} \begin{bmatrix} 1 & \hat{a}/2 & 0 & 0 \\ \hat{a}/2 & \hat{a}^2/4 & 0 & 0 \\ 0 & 0 & 1 & -\hat{a}/2 \\ 0 & 0 & -\hat{a}/2 & \hat{a}^2/4 \end{bmatrix}, \quad (\text{A.10})$$

$$\mathbf{C}_e = \frac{R_L}{2} \begin{bmatrix} 1 & \hat{a}/2 & 0 & 0 \\ \hat{a}/2 & \hat{a}^2/4 & 0 & 0 \\ 0 & 0 & 1 & -\hat{a}/2 \\ 0 & 0 & -\hat{a}/2 & \hat{a}^2/4 \end{bmatrix} + \frac{R_T}{2} \begin{bmatrix} 0 & 0 & 0 & 0 \\ 0 & 1 & 0 & 0 \\ 0 & 0 & 0 & 0 \\ 0 & 0 & 0 & 1 \end{bmatrix} + R_C \begin{bmatrix} 0 & 0 & 0 & 0 \\ 0 & 1 & 0 & -1 \\ 0 & 0 & 0 & 0 \\ 0 & -1 & 0 & 1 \end{bmatrix} \quad (\text{A.11})$$

and

$$\mathbf{K}_e = \frac{4}{\hat{a}^2 C_0} \begin{bmatrix} 1 & \frac{\hat{a}}{2} & -1 & \frac{\hat{a}}{2} \\ \frac{\hat{a}}{2} & \frac{\hat{a}^2}{4} \frac{C+2C_0}{C+C_0} & -\frac{\hat{a}}{2} & \frac{\hat{a}^2}{4} \frac{C}{C+C_0} \\ -1 & -\frac{\hat{a}}{2} & 1 & -\frac{\hat{a}}{2} \\ \frac{\hat{a}}{2} & \frac{\hat{a}^2}{4} \frac{C}{C+C_0} & -\frac{\hat{a}}{2} & \frac{\hat{a}^2}{4} \frac{C+2C_0}{C+C_0} \end{bmatrix}. \quad (\text{A.12})$$

Note that a capacitance C_0 appears in Eq. (A.12) while it is not shown in Fig. 1. As fully explained in [25], C_0 is a numerical parameter that is required to relax some constraints in the electrical network in order to allow the definition of a stiffness matrix. To limit the influence of this additional degree of freedom on the results, C_0 that has to be small compared to C . A deeper analysis on the influence of this numerical parameter is out of the scope of this work but it can be shown that a value $C_0 = C \times 10^{-3}$ is adequate for the present calculations.

Once all the matrices in Eq. (12) have been defined, a last step consists in a reorganizing the degrees of freedom from the following permutation that collect left and right degrees of freedom (\mathbf{q}_L and \mathbf{q}_R) without separating mechanical and electrical ones:

$$\begin{bmatrix} \mathbf{q}_L \\ \mathbf{q}_R \end{bmatrix} = \begin{bmatrix} W_L \\ \theta_L \\ q_{wL} \\ q_{\theta L} \\ W_R \\ \theta_R \\ q_{wR} \\ q_{\theta R} \end{bmatrix} = \begin{bmatrix} \mathbf{I} & \mathbf{0} & \mathbf{0} & \mathbf{0} \\ \mathbf{0} & \mathbf{0} & \mathbf{I} & \mathbf{0} \\ \mathbf{0} & \mathbf{I} & \mathbf{0} & \mathbf{0} \\ \mathbf{0} & \mathbf{0} & \mathbf{0} & \mathbf{I} \end{bmatrix} \begin{bmatrix} W_L \\ \theta_L \\ W_R \\ \theta_R \\ q_{wL} \\ q_{\theta L} \\ q_{wR} \\ q_{\theta R} \end{bmatrix}. \quad (\text{A.13})$$

Using this permutation matrix on the matrices in Eq. (12) finally provides the one-dimensional electromechanical finite element that can be used with an assembly process in order to define the finite element model of the whole structure.

References

- [1] C. Foasso, Quand l'informatique était analogique [When computing was analog], *Pour la Science* (522) (2021).
- [2] R.H. MacNeal, The Solution of Partial Differential Equations by Means of Electrical Networks (Ph.D. thesis), California Institute of Technology, 1949.
- [3] G. McCann, The California Institute of Technology electric analog computer, *Math. Tables Other Aids Comput.* 3 (28) (1949) 501–513.
- [4] R. MacNeal, G. McCann, C. Wilts, The solution of aeroelastic problems by means of electrical analogies, *J. Aeronaut. Sci.* 18 (12) (1951) 777–789.
- [5] R. MacNeal, C. McCormick, The NASTRAN computer program for structural analysis, *Comput. Struct.* 1 (3) (1971) 389–412.
- [6] D. Wagg, K. Worden, R. Barhorpe, P. Gardner, Digital twins: state-of-the-art and future directions for modeling and simulation in engineering dynamics applications, *ASCE-ASME J. Risk Uncertain. Eng. Syst Part B: Mech. Eng.* 6 (3) (2020).
- [7] S. Vidoli, F. dell'Isola, Vibration control in plates by uniformly distributed PZT actuators interconnected via electric networks, *Eur. J. Mech. A Solids* 20 (3) (2001) 435–456.
- [8] S. Alessandroni, F. dell'Isola, M. Porfiri, A revival of electric analogs for vibrating mechanical systems aimed to their efficient control by PZT actuators, *Int. J. Solids Struct.* 39 (20) (2002) 5295–5324.
- [9] M. Porfiri, F. dell'Isola, F. Frattale Mascioli, Circuit analog of a beam and its application to multimodal vibration damping, using piezoelectric transducers, *Int. J. Circuit Theory Appl.* 32 (4) (2004) 167–198.
- [10] B. Lossouarn, J.-F. Deü, M. Aucejo, Multimodal vibration damping of a beam with a periodic array of piezoelectric patches connected to a passive electrical network, *Smart Mater. Struct.* 24 (11) (2015) 115037.
- [11] R. Darleux, B. Lossouarn, J.-F. Deü, Broadband vibration damping of non-periodic plates by piezoelectric coupling to their electrical analogues, *Smart Mater. Struct.* 29 (5) (2020) 054001.
- [12] R. Darleux, Development of Analogous Piezoelectric Networks for the Vibration Damping of Complex Structures (Ph.D. thesis), HESAM Université, 2020.
- [13] P. Soltani, G. Kerschen, The nonlinear piezoelectric tuned vibration absorber, *Smart Mater. Struct.* 24 (7) (2015) 075015.
- [14] B. Lossouarn, J.-F. Deü, G. Kerschen, A fully passive nonlinear piezoelectric vibration absorber, *Phil. Trans. R. Soc. A* 376 (2127) (2018) 20170142.
- [15] G. Raze, B. Lossouarn, A. Paknejad, G. Zhao, J.-F. Deü, C. Collette, G. Kerschen, A multimodal nonlinear piezoelectric vibration absorber, in: *Proceedings of ISMA2018 and USD2018*, KU Leuven, 2018, pp. 63–77.
- [16] G. Raze, A. Jadoul, S. Guichaux, V. Broun, G. Kerschen, A digital nonlinear piezoelectric tuned vibration absorber, *Smart Mater. Struct.* 29 (1) (2019) 015007.
- [17] G. Habib, G. Kerschen, A principle of similarity for nonlinear vibration absorbers, *Physica D* 332 (2016) 1–8.
- [18] N.W. Hagood, A. von Flotow, Damping of structural vibrations with piezoelectric materials and passive electrical networks, *J. Sound Vib.* 146 (2) (1991) 243–268.
- [19] O. Thomas, J. Ducarne, J.-F. Deü, Performance of piezoelectric shunts for vibration reduction, *Smart Mater. Struct.* 21 (1) (2011) 015008.
- [20] P. Soltani, G. Kerschen, G. Tondreau, A. Deraemaeker, Piezoelectric vibration damping using resonant shunt circuits: An exact solution, *Smart Mater. Struct.* 23 (12) (2014) 125014.
- [21] S.-Y. Wu, Method for multiple mode piezoelectric shunting with single PZT transducer for vibration control, *J. Intell. Mater. Syst. Struct.* 9 (12) (1998) 991–998.
- [22] G. Raze, A. Paknejad, G. Zhao, C. Collette, G. Kerschen, Multimodal vibration damping using a simplified current blocking shunt circuit, *J. Intell. Mater. Syst. Struct.* 31 (14) (2020) 1731–1747.

- [23] A. Fleming, S. Behrens, S. Moheimani, Reducing the inductance requirements of piezoelectric shunt damping systems, *Smart Mater. Struct.* 12 (1) (2003) 57.
- [24] J. Ducarne, O. Thomas, J.-F. Deü, Placement and dimension optimization of shunted piezoelectric patches for vibration reduction, *J. Sound Vib.* 331 (14) (2012) 3286–3303.
- [25] B. Lossouarn, M. Aucejo, J.-F. Deü, Electromechanical wave finite element method for interconnected piezoelectric waveguides, *Comput. Struct.* 199 (2018) 46–56.
- [26] B. Zhou, F. Thouverez, D. Lenoir, Essentially nonlinear piezoelectric shunt circuits applied to mistuned bladed disks, *J. Sound Vib.* 333 (9) (2014) 2520–2542.
- [27] T.M. Silva, M.A. Clementino, C. De Marqui Jr, A. Erturk, An experimentally validated piezoelectric nonlinear energy sink for wideband vibration attenuation, *J. Sound Vib.* 437 (2018) 68–78.
- [28] T. Detroux, G. Habib, L. Masset, G. Kerschen, Performance, robustness and sensitivity analysis of the nonlinear tuned vibration absorber, *Mech. Syst. Signal Process.* 60 (2015) 799–809.
- [29] E. Gluskin, The use of non-linear capacitors, *Int. J. Electron.* 58 (1) (1985) 63–81.
- [30] E. Gluskin, A nonlinear resistor and nonlinear inductor using a nonlinear capacitor, *J. Franklin Inst. B* 336 (7) (1999) 1035–1047.
- [31] C. Maurini, J. Pouget, F. dell’Isola, On a model of layered piezoelectric beams including transverse stress effect, *Int. J. Solids Struct.* 41 (16–17) (2004) 4473–4502.